


## Toward flying qubit spectroscopy

Benoît Rossignol, Thomas Kloss, Pacôme Armagnat, and Xavier Waintal  
*Université Grenoble Alpes, CEA, INAC-Pheliqs, 38000 Grenoble, France*

 (Received 16 February 2018; revised manuscript received 11 June 2018; published 15 November 2018)

While the coherent control of two-level quantum systems, qubits, is now standard, their continuum electronic equivalents, flying qubits, are much less developed. The first step in this direction has been achieved in dc interferometry experiments. Here, we propose a simple setup to perform the second step, the spectroscopy of these flying qubits, by measuring the dc response to a high-frequency ac voltage drive. Using two different concurring approaches (Floquet theory and time-dependent simulations) and three different models (an analytical model, a simple microscopic model, and a realistic microscopic model), we predict the power-frequency map of the multiterminal device. We argue that this spectroscopy provides a direct measurement of the flying qubit characteristic frequencies and a key validation for more advanced quantum manipulations.

DOI: [10.1103/PhysRevB.98.205302](https://doi.org/10.1103/PhysRevB.98.205302)

### I. INTRODUCTION

The development of a new type of quantum bit happens in stages. Let us consider the singlet-triplet double-quantum-dot qubit [1] as a typical example. In this case, the first stage consists of dc measurements of the so-called stability diagram. Once a suitable physical regime has been found, the second stage consists of performing the spectroscopy of the qubit to assert its suitability and determine its dynamical characteristics. This can be done through, e.g., electronic dipolar spin resonance [2]. It is crucial to pass these two stages before one can consider sending more elaborate pulse sequences like Rabi, Ramsey, and echo experiments. In the last stage (before considering coupling several of these qubits), one implements single-shot measurements.

Quantum mechanics, however, is not limited to bound states, and propagating quantum states instead of bound states could also be used to form qubits. The so-called flying qubits have been successfully realized with photons in linear quantum optics [3,4], but here, we focus on proposals based on electrons [5]. The first stage of the electronic flying qubit [6,7] implementation has been demonstrated in several experiments that show controlled two-path interferometry in a two-dimensional electron gas in the presence [8,9] or absence [10,11] of magnetic field as well as in graphene [12]. Other features, specific to propagating quantum systems, have also been demonstrated (including single-electron sources [13–16] and their Hong-Ou-Mandel characterization) or proposed theoretically [17–19]. However, the second stage, the spectroscopy of a flying qubit, has not yet been realized experimentally.

The electronic flying qubits that we consider in this paper are “two-path” interferometers, the electronic analog of the Mach-Zehnder interferometer studied in optics. The two states of the qubits are coded in the two paths,  $\uparrow$  and  $\downarrow$ , that a single electronic excitation uses for propagation. Here, the role of the qubit frequency is replaced by  $\hbar/\tau$ , where  $\tau$  is a characteristic time, the difference between two times of flight (to be defined below), of the device. Like in a localized system that may have

multiple energy levels, there may be several propagating channels, giving rise to several characteristic times  $\tau$ . Measuring these times and assessing whether electronic interferometry experiments can be performed at high frequency are the next key milestone of the field.

In this paper, we propose to use quantum rectification (measurement of a dc current in the presence of a high-frequency sinusoidal drive) [20–25] as a tool to perform the spectroscopy of flying qubits. We argue that quantum rectification provides a clear spectroscopy of the device while being much more accessible experimentally than other techniques, in particular in the challenging  $\sim 10$  GHz–1 THz frequency range which is required for this type of physics.

### II. A TWO-PATH ELECTRONIC INTERFEROMETER USING A SPLIT-WIRE GEOMETRY

We focus this study on the tunneling wire “flying qubit” geometry sketched in Fig. 1(a) and studied experimentally in [10,11,26,27]. The device consists of two quasi-one-dimensional wires labeled  $\uparrow$  (upper) and  $\downarrow$  (lower) connected to four electrodes: two on the left,  $L \uparrow$  and  $L \downarrow$ , and two on the right,  $R \uparrow$  and  $R \downarrow$ . Close to the electrodes, the wires are disconnected. However, in a central region of length  $\mathcal{L}$ , the two wires are in contact, so that an electron can tunnel back and forth from the upper to the lower part. A capacitive top gate  $V_g$  controls the intensity of the tunneling coupling between the wires. The coherent oscillation that takes place in the tunneling region between the upper and lower wires can be interpreted as a quantum gate operated on the flying qubit. Equivalently, an electron entering the upper wire decomposes into a superposition of symmetric and antisymmetric propagating states, which forms a two-path interferometer.

The dc characteristics of this device were analyzed previously [10,28] both theoretically and experimentally. For completeness, we recall here its salient features. Let us determine the scattering matrix of this device in the limit where (i) there is only one propagating channel in each of the wires and (ii) the spatial variation of the tunneling coupling is very

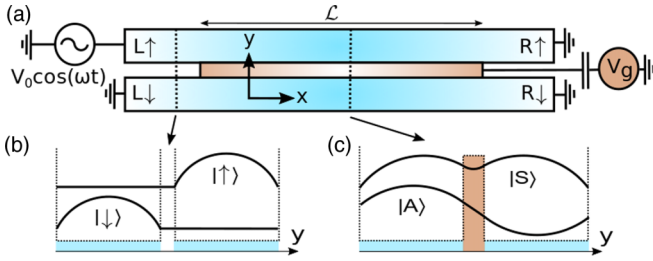


FIG. 1. (a) Schematic of the flying qubit geometry. Two wires labeled  $\uparrow, \downarrow$  are connected to two electrodes on the left ( $L \uparrow, L \downarrow$ ) and two electrodes on the right ( $R \uparrow, R \downarrow$ ). Schematics of the transverse part of the propagating modes (b) close to the electrodes and (c) in the central tunneling region.

smooth with respect to the Fermi wavelength. This implies that there is no reflection in the device as backscattering involves the  $2k_F$  Fourier component of the potential ( $k_F$  is the Fermi momentum): an electron injected on the left, say, in  $L \uparrow$ , is transmitted toward either  $R \uparrow$  or  $R \downarrow$ . To determine the transmission amplitude  $d_{ba}(E)$  from channel  $a$  on the left to channel  $b$  on the right ( $a, b \in \{\uparrow, \downarrow\}$ ), let us consider the transverse part of the propagating modes. A schematic representation of these wave functions is shown in Fig. 1(b) for the decoupled wires (close to the electrodes) and in Fig. 1(c) for the tunneling region. In the latter, the  $\uparrow$  and  $\downarrow$  channels hybridize into symmetric ( $S$ ) and antisymmetric ( $A$ ) channels of respective longitudinal momenta  $k_S$  and  $k_A$  along the  $x$  direction. The key point is to recognize that the  $S$  ( $A$ ) channel is continuously connected to the symmetric (antisymmetric) combination of the  $\uparrow$  and  $\downarrow$  channels,  $|S/A\rangle \leftrightarrow (|\uparrow\rangle \pm |\downarrow\rangle)/\sqrt{2}$ . Hence, an electron injected in  $|\uparrow\rangle$ ,

$$|\uparrow\rangle = \frac{1}{2}(|\uparrow\rangle + |\downarrow\rangle) + \frac{1}{2}(|\uparrow\rangle - |\downarrow\rangle) \rightarrow \frac{1}{\sqrt{2}}(|S\rangle + |A\rangle), \quad (1)$$

is transmitted into  $S$  and  $A$  with amplitude  $1/\sqrt{2}$ . Inside the tunneling wire, the wave function picks up a phase  $e^{i\phi_{S/A}}$ , which in the Wentzel-Kramers-Brillouin (WKB) approximation reads  $\phi_{S/A} = \int_0^{\mathcal{L}} dx k_{S/A}(x) \approx k_{S/A}\mathcal{L}$ . After the tunneling region,  $S$  and  $A$  recombine into the  $\uparrow$  and  $\downarrow$  channels, and we arrive at

$$d_{\uparrow\uparrow}(E) = \frac{1}{2}(e^{i\phi_S} + e^{i\phi_A}), \quad d_{\downarrow\uparrow}(E) = \frac{1}{2}(e^{i\phi_S} - e^{i\phi_A}). \quad (2)$$

The differential conductance  $g_{ba}$  that relates the current flowing on the right in lead  $b$  from an increase of voltage in the left on lead  $a$  is given by the Landauer formula,  $g_{ba} = (e^2/h)D_{ba}(E_F)$ , with  $D_{ba}(E_F) = |d_{ba}(E_F)|^2$  and  $E_F$  being the Fermi energy (we ignore spin everywhere; it can be restored by simply multiplying the currents by a factor of 2). The above analytic expressions have been shown to grasp the important features of the corresponding experimental devices in dc [10]. In particular, upon decreasing the gate voltage  $V_g$  toward large negative values,  $k_S - k_A$  decreases toward zero (the two channels become increasingly alike), and the differential conductance  $g_{\uparrow\uparrow} \propto \cos^2[(\phi_S - \phi_A)/2] \approx \cos^2[(k_S - k_A)\mathcal{L}/2]$  first oscillates, then saturates to perfect transmission.

For the ac response discussed in this paper, we need the energy dependence of the transmission amplitude. Linearizing the dispersion relation of the  $S$  and  $A$  channels, we introduce the corresponding velocity  $v_{S,A} = (1/\hbar)dE_{S,A}/dk$  and the time of flight  $\tau_{S/A} = \mathcal{L}/v_{S,A}$  through the channel. The phase difference  $\phi_S(E) - \phi_A(E)$  is controlled by the difference  $\tau \equiv \tau_S - \tau_A$  of the times of flight, and we arrive at

$$\phi_S(E) - \phi_A(E) \approx \delta_F + (E - E_F)\tau/\hbar, \quad (3)$$

with  $\delta_F \equiv \phi_S(E_F) - \phi_A(E_F)$ .

### III. A GENERAL FORMULA FOR CALCULATING RECTIFICATION CURRENTS

We now develop the scattering theory of the rectified direct current generated by an ac voltage drive. We consider a multiterminal mesoscopic system and apply a periodic time-dependent voltage  $V(t)$  to one electrode (for definiteness, we focus below on  $L \uparrow$ ) with frequency  $\omega$ . We seek to obtain the average (over time) dc current flowing in the different electrodes. Such a calculation can be performed in different but fully equivalent ‘‘Floquet’’ formalisms, including the scattering [29], nonequilibrium Green’s function [30], and wave function approach [31]. Here, we follow the latter after Refs. [19,31].

In what follows, we neglect the spatial dependence of the electric potential drop; that is, we suppose that the drop in electric potential takes place very abruptly at the Ohmic contact–two-dimensional gas interface. Such an approximation is well justified in the present case due to the presence of the electrostatic gates that define the conducting region. These gates are metallic and hence equipotential; they ensure that the potential drop takes place over a distance which is essentially set by the distance between the gate and the two-dimensional electron gas. This distance is typically of the order of 100 nm, which is much shorter than the size of the device (typically,  $10 \mu\text{m}$ ), so that the approximation of a perfectly sharp drop is reasonably accurate. In the opposite situation (the absence of electrostatic gates) the potential drop would be linear between the two contacts. A discussion of this problem can be found in Sec. 8.4 of [31]. The abrupt drop in potential is an important ingredient for the physics of propagating pulses such as the minimum excitations, ‘‘levitons.’’ The recent experiments that measured the time of flight of such pulses [32] provided clear experimental evidence that the drop is indeed sharp and takes place at the Ohmic contact–electron gas interface since well-defined velocities could be measured.

The effect of the time-dependent voltage is to dress an incoming wave function of the form  $e^{ikx - iEt/\hbar}$  with an extra phase factor  $e^{-i\Phi(t)}$  [with  $\Phi(t) \equiv \int_0^t dt' eV(t')/\hbar$ ] that accounts for the variation of electric potential. Decomposing this phase into its Fourier component  $P_n$ ,

$$e^{-i\Phi(t)} = \sum_n P_n e^{-i\omega nt}, \quad (4)$$

the net effect of  $V(t)$  is that the incoming wave function is now a coherent superposition  $\sum_n P_n e^{ikx - iEt/\hbar - i\omega nt}$  of plane waves at different energies. As different energies get transmitted into different channels, we arrive at the following time-dependent transmission amplitude for an incoming

energy  $E$ :

$$d_{ba}(t, E) = \sum_n P_n d_{ba}(E + n\hbar\omega) e^{-iEt/\hbar - i\omega t}, \quad (5)$$

where  $d_{ba}(t, E)$  is the Fourier transform with respect to  $E'$  of  $d_{ba}(E', E)$ , which is itself the inelastic amplitude to be transmitted from energy  $E$  of lead  $a$  toward energy  $E'$  of lead  $b$ . The generalization of the Landauer formula to time-dependent currents provides the time-dependent current  $I_b(t)$  as

$$I_b(t) = \frac{e}{\hbar} \int \frac{dE}{2\pi} [|d_{ba}(t, E)|^2 - |d_{ba}(E)|^2] f_a(E), \quad (6)$$

where  $f_a(E)$  is the Fermi function of lead  $a$  subject to the time-dependent voltage. The second term in the previous equation subtracts the current sent from lead  $a$  in the absence of time-dependent voltage, which is a convenient way to ensure the overall current conservation [17,31]. Focusing on the dc (rectification) current  $\bar{I}_b = \omega/(2\pi) \int_0^{2\pi/\omega} dt I_b(t)$ , we arrive at

$$\bar{I}_b = \frac{e}{\hbar} \sum_n |P_n|^2 \int dE |d_{ba}(E)|^2 [f_a(E + n\hbar\omega) - f_a(E)]. \quad (7)$$

Equation (7) is very general and relates the rectification properties of an arbitrary mesoscopic system to its scattering matrix  $d_{ba}(E)$ , a well-known dc object. In particular, it can be easily evaluated numerically for a large class of microscopic models using readily available numerical packages (in our case the KWANT [33] package) for arbitrary periodic pulses. We note that following the same arguments as in Ref. [31], we find that the rectification current is ‘‘conserved’’ and ‘‘gauge invariant’’ in the sense defined by Buttiker *et al.* [34]; that is, the dc current in electrode  $a$  is exactly compensated by the dc currents in the other leads, and applying an ac potential on all the leads simultaneously does not generate any dc current.

## IV. APPLICATION TO THE FLYING QUBIT

### A. Simple scattering model

We now make a specific calculation using our analytical model (2) for the flying qubit geometry. We also specialize to a drive  $V(t) = V_0 \cos \omega t$  with a unique frequency which implies  $P_n = J_n(eV_0/\hbar\omega)$ , where  $J_n(x)$  is the Bessel function of the first kind. Up to an irrelevant phase factor, the time-dependent transmission reads

$$d_{\uparrow\uparrow}(t, E) = \frac{1}{2} [1 + e^{i\delta_F + i\tau(E - E_F)/\hbar} e^{i\Phi(t)} e^{-i\Phi(t - \tau)}]. \quad (8)$$

Following the same route as in the general case and assuming zero temperature for simplicity, we get

$$\bar{I}_{\uparrow} = \frac{e}{4\pi\tau} \sin(\delta_F) \left\{ J_0 \left[ \frac{2eV_0}{\hbar\omega} \sin \left( \frac{\omega\tau}{2} \right) \right] - 1 \right\}, \quad (9a)$$

$$\bar{I}_{\downarrow} = -\bar{I}_{\uparrow}. \quad (9b)$$

Equations (9a) and (9b) call for a few comments. (i) Even though we apply the oscillatory voltage on the upper left electrode, no dc current actually flows there as implied by Eq. (9b) and current conservation. Instead, the dc rectified

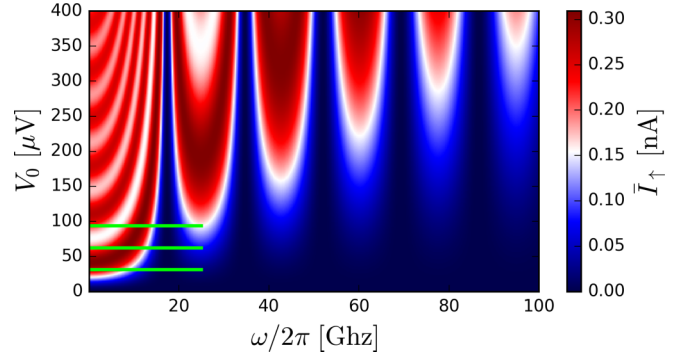


FIG. 2. Rectified dc current from Eq. (9a) for  $\delta_F = 0.32\pi$  and  $\tau = 58$  ps. The results of Fig. 4 correspond to cuts along the green lines.

current is pumped from the upper right to the lower right electrode. (ii) Equation (9a) is nonperturbative with respect to both frequency and drive amplitude. An illustrative color plot is shown in Fig. 2. It shows rich oscillatory features as a function of both  $\omega$  and  $V_0$ . Figure 2 is the flying qubit analog of the usual spectroscopy maps. (iii) The adiabatic limit  $\omega \rightarrow 0$  can be understood without using the time-dependent Floquet formalism. First, we compute the dc current-voltage characteristics

$$\begin{aligned} I(V) &= (e/h) \int_{E_F}^{E_F + eV} dE |d_{\uparrow\uparrow}(E)|^2 \\ &= \frac{e^2}{2h} V + \frac{e}{2\pi\tau} \sin \left( \frac{eV\tau}{2\hbar} \right) \cos \left( \delta_F + \frac{eV\tau}{2\hbar} \right). \end{aligned} \quad (10)$$

Then the adiabatic rectified dc current is found by computing the time average of  $I(V = V_0 \cos \omega t)$ , and we arrive at

$$\bar{I}_{\uparrow} = \frac{e}{4\pi\tau} \sin(\delta_F) \left[ J_0 \left( \frac{eV_0\tau}{\hbar} \right) - 1 \right], \quad (11)$$

which corresponds to the  $\omega \rightarrow 0$  limit of Eq. (9a). The rectified current is directly linked to the presence of the non-linear term in the  $I(V)$  characteristics. (iv) At large  $x$ , the Bessel function decreases as  $J_0(x) \sim \sin(x + \pi/4) \sqrt{2/\pi x}$ , so that the rectified current reaches its maximum value  $\bar{I}_{\uparrow} = -\frac{e}{4\pi\tau} \sin(\delta_F)$  at large voltage and  $\omega\tau = \pi$ .

### B. Simple microscopic model

We now introduce a microscopic model for the Mach-Zehnder interferometer of Fig. 1 and discuss our direct method to perform time-dependent simulations of the device. We shall find a perfect match between our time-dependent simulations and a semianalytical approach that uses the microscopic model to calculate the dc scattering matrix (using the KWANT package [33]) and Eq. (7) to relate the latter to the rectified current in the presence of an ac drive. We model the Mach-Zehnder interferometer through the following Hamiltonian:

$$\begin{aligned} \hat{H}(t) &= \sum_{a \in \{\uparrow, \downarrow\}} \sum_{i=-\infty}^{+\infty} [-c_{i+1,a}^\dagger c_{i,a} + U_i c_{i,a}^\dagger c_{i,a}] \\ &\quad + \sum_{i=-L/2}^{+L/2} \gamma_i c_{i,\uparrow}^\dagger c_{i,\downarrow} + \text{H.c.}, \end{aligned} \quad (12)$$

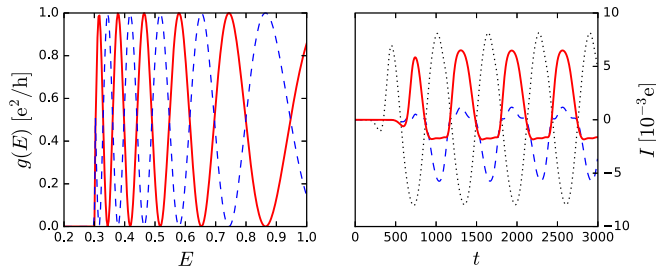


FIG. 3. Simple microscopic model. Left: dc differential conductances  $g_{\uparrow\uparrow}(E)$  (dashed blue line) and  $g_{\downarrow\uparrow}(E)$  (solid red line) as obtained from a direct numerical calculation of the tight-binding model. The numerical calculations were performed with the KWANT [33] package. The reflection probability from  $L \uparrow$  to  $L \uparrow$  or  $L \downarrow$  vanishes in the region of interest. Right: currents in  $R \downarrow$  [solid red line,  $I_{\downarrow}(t)$ ] and  $R \uparrow$  [dashed blue line,  $I_{\uparrow}(t)$ ] after a microwave excitation in  $L \uparrow$  (dotted black line) computed using time-dependent simulations of the microscopic model.

where  $c_{i,a}$  ( $c_{i,a}^\dagger$ ) is the usual fermionic destruction (creation) operator on site  $i$  and wire  $a \in \{\uparrow, \downarrow\}$ .  $U_i$  is an electric potential present in the central region,  $\gamma_i$  characterizes the tunneling between the upper and lower wires and is controlled by the voltage  $V_g$ , and  $L$  is the total length of the tunneling part of the wire. The nearest-neighbor hopping amplitude is set to unity, which defines our energy and time units ( $\hbar = 1$ ).

For our simulations, we choose  $L = 500$  sites,  $E_F = 1.3$ , and  $\gamma_i$  interpolates smoothly (over 50 sites) between zero in the electrodes and  $-0.7$  in the tunneling region. The potential  $U_i$  interpolates smoothly between 0.8 in the electrode and 1 in a small region just before and after the tunneling region (this region is present for numerical convenience; see Sec. 10 of Ref. [31]) and vanishes inside the tunneling region.  $U_i$  also includes a uniform contribution  $V_0 \cos(\omega t)$  for all sites in the upper left electrode and  $t > 0$ . For these parameters, we find a characteristic time  $\tau \approx 58$  and  $\delta_F \approx 0.32\pi$ . These two values can be determined consistently from three different calculations: from the propagation of a voltage pulse in the time-dependent simulation, from the energy dependence of the dc conductance, and from the WKB approximation.

The time-dependent simulations are performed using the method described in Refs. [31,35], in which all details are provided. In this method, we directly integrate the Schrödinger equation

$$i\hbar\partial_t|\Psi(t)\rangle = \hat{H}(t)|\Psi(t)\rangle \quad (13)$$

without further approximations. The main difference from Eq. (7) lies in the treatment of the oscillatory ac potential: in the scattering matrix approach, it is assumed that the ac potential drop does not create any backscattering. This approximation is usually very good, up to small deviations of  $\sim V_0/E_F$  that were calculated in Ref. [31]. The left panel of Fig. 3 shows an example of the dc differential conductances  $g_{\uparrow\uparrow}(E)$  and  $g_{\downarrow\uparrow}(E)$  as obtained from a direct numerical calculation of the tight-binding “simple microscopic model”. We indeed observe the oscillations with energy discussed after Eq. (2). We checked that the period of these oscillations matches the WKB result that can be calculated independently. The right panel of Fig. 3 shows the result [current  $I(t)$  versus

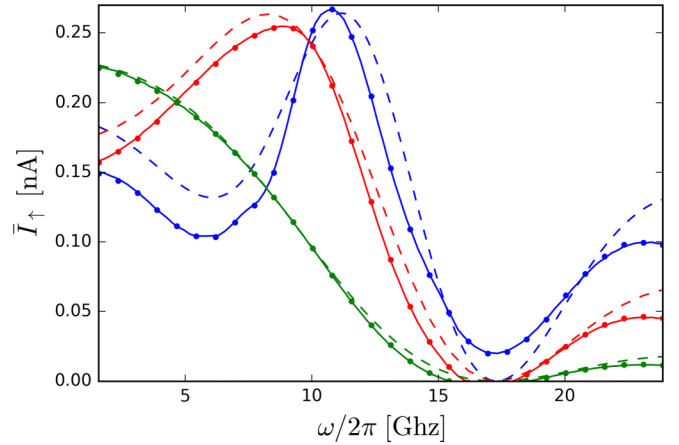


FIG. 4. Simple microscopic model. The dc current  $\bar{I}_{\uparrow}$  for three different voltage amplitudes  $V(t) = V_0 \cos(\omega t)$  with  $V_0 = 31, 62, 93 \mu\text{V}$  (green, red, and blue lines, respectively). The symbols correspond to a time-dependent simulation of Eq. (12), the solid lines correspond to semianalytic theory (7), and the dashed lines correspond to the analytic approach (9a).

time  $t$ ] of a typical time-dependent simulation of the model in the presence of the ac drive (smoothly switched on at  $t = 0$ ). These curves are averaged over time to calculate the dc rectification current  $\bar{I}$ .

### C. Comparison between the different approaches

The first remarkable feature of the rectified current is the fact that it is pumped between the two right electrodes. The dc current in electrode  $L \uparrow$  vanishes even though the ac voltage is applied there. Figure 2 shows the rectified current (9a) as a function of the drive frequency and amplitude.

The dc current follows damped oscillations with both  $V_0$  and  $\omega$  with frequency  $h/\tau$  in the  $\sim 10$ -GHz range. In particular, the characteristic time  $\tau$  can be extracted directly from the minima of the dc current as a function of  $\omega$ . Figure 4 shows the plot of current  $\bar{I}_{\uparrow}$  versus frequency  $\omega$  for three different values of  $V_0$ , corresponding to cuts in Fig. 2 (green lines). Figure 4 contains the results of three different calculations: the ideal analytical calculation (9a), the time-dependent simulations of the microscopic model (12), and a semianalytical calculation that uses the time-independent part of the microscopic model and computes the rectification properties using Eq. (7). We find close agreement among the three approaches, with a very accurate agreement between the latter two. Departure from the ideal analytic formula (9a) arises due to the presence of a small backscattering in the device (which is not perfectly adiabatic) and the fact that the linear relation (3) is not strictly valid in the microscopic model (the presence of the other characteristic scales).

We conclude that the ideal analytical model (9a) describes the physics qualitatively but cannot be used for quantitative predictions. On the other hand, Eq. (7) is computationally affordable and in precise agreement with the direct integration of the Schrödinger equation. It may be used for other, more realistic models, which we shall do in the next section.



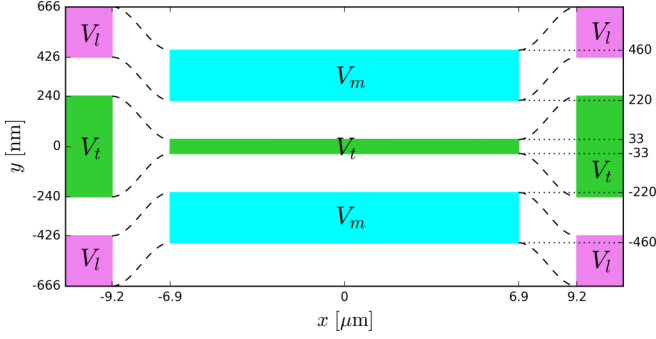


FIG. 5. Top view of the layout of the gates that define the realistic microscopic model.

### V. REALISTIC MICROSCOPIC MODEL

The two models studied above are, of course, idealized. Below, we develop a much more refined model which builds upon our previous work [10]. The model of Ref. [10] was shown to be in remarkable agreement with the dc experimental data even though the electrostatic potential was modeled rather crudely. Here, we extend the modelization and perform a self-consistent treatment of the electrostatic-quantum problem. We also include finite-temperature thermal smearing ( $\sim 20$  mK).

Before describing the specifics of the “realistic model,” let us briefly discuss some orders of magnitude. The typical value of the difference of the time of flight  $\tau$  that can be reached experimentally depends on the product of three factors,  $\tau = \mathcal{L}(1/v_S - 1/v_A) \approx ((k_S - k_A)/k_S)\mathcal{L}/v_S$ . The longitudinal velocity  $v_S$  can be estimated from the experimental results of Ref. [32] to be  $v_S \approx (2-5) \times 10^5$  m s $^{-1}$ . Typical values of  $k_S - k_A$  found in Ref. [10] lie between 1% and up to 10% of the Fermi momentum  $k_S$ . The length  $\mathcal{L}$  of the tunneling region in Ref. [10] was  $\mathcal{L} = 1 \mu\text{m}$ , but coherent oscillations have since been observed in much longer samples [36],  $\mathcal{L} \approx 40 \mu\text{m}$ , indicating that the low-temperature ( $\approx 20$  mK) phase coherence length in these samples is of a few tens of micrometers, comparable to what has been observed in the quantum Hall regime [9]. Altogether, we estimate  $\tau \sim 100$  ps for the slowest mode of a 20- $\mu\text{m}$ -long sample, which is consistent with what is found below in the simulations of the realistic model.

#### A. Geometry

The model is defined solely by the position of the top gates that are deposited on the surface of the GaAs heterostructure. It consists of a central region (defined by two lateral gates and a central tunneling gate) which smoothly evolves into two disconnected wires on the left and on the right of the central region. A top view of the layout of the gates is shown in Fig. 5. A cut at  $x = 0$  (left panel) and  $x > 10 \mu\text{m}$  (right panel) is shown in the top row of Fig. 6.

The dimensions of the device (with a central region  $13.8 \mu\text{m}$  long and  $0.92 \mu\text{m}$  wide) are fully compatible with standard electron-beam lithography techniques. The different gates are grouped into three categories: the three interior gates (green) are set to the same potential  $V_l$ , the two outer gates

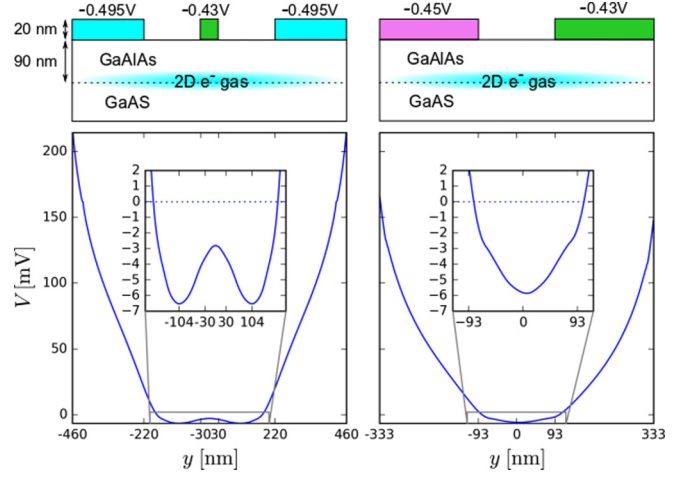


FIG. 6. Top: side view of the realistic microscopic model layout. Bottom: self-consistent electrostatic potential seen by the electrons as a function of the transverse direction  $y$ . The insets show a zoom close to the Fermi level  $E_F = 0$ . Left: cut inside the central region ( $x = 0$ ). Right: cut inside the leads ( $x > 10 \mu\text{m}$  or  $x < 10 \mu\text{m}$ )

of the central region are set to  $V_m$ , and the four outer gates of the electrodes are set to  $V_l$ . The transition region between the central region and the lead ( $x \in [-9.2, -6.9]$  and  $x \in [6.9, 9.2] \mu\text{m}$ ) is defined by an interpolation described later in this section.

#### B. Self-consistent model

In order to calculate the electrostatic potential seen by the two-dimensional electron gas, we work in the effective-mass ( $m^* = 0.067m_e$ , where  $m_e$  is the bare electron mass) approximation for the Schrödinger equation, which is solved self-consistently with Poisson’s equation. The Hamiltonian of the two-dimensional electron gas,

$$H = \frac{P_x^2 + P_y^2}{2m^*} - eV(x, y, z = 0), \quad (14)$$

is discretized on a square grid with lattice constant  $a = 3$  nm (approximately  $2 \times 10^6 \approx 300 \times 6000$  sites). The Schrödinger equation

$$H\Psi_{\alpha E} = E\Psi_{\alpha E} \quad (15)$$

is solved using the KWANT package [33]. The electrodes are taken to be semi-infinite, so that the spectrum is actually continuous and the eigenfunctions are labeled by an energy  $E$  and a mode index  $\alpha$ . The density of electrons  $n(x, y)$  is given by the integral over energy of the local density of states,

$$n(x, y) = \sum_{\alpha} \int \frac{dE}{2\pi} |\Psi_{\alpha E}(x, y)|^2 f(E), \quad (16)$$

where  $f(E) = 1/(e^{E/k_B T} + 1)$  is the Fermi function at temperature  $T$  (and we have set the Fermi energy  $E_F = 0$  as our reference energy point). The Poisson equation away from the electron gas reads

$$\Delta V(x, y, z) = 0, \quad (17)$$

while close to the gas the discontinuity of the electric field is set by  $n(x, y)$ :

$$\partial_z V(x, y, 0^+) - \partial_z V(x, y, 0^-) = -\frac{e}{\epsilon} [n(x, y) + n_d], \quad (18)$$

where the dopant density  $n_d$  sets the actual density of the gas and  $\epsilon \approx 12\epsilon_0$  is the dielectric constant. The Poisson equation is solved using the FENICS package [37].

In order to solve the set of self-consistent equations (15), (16), (17), and (18), we perform one approximation which considerably lowers the computational effort while retaining good accuracy. In a first step, we solve the self-consistent problem deep in the lead region where the system is invariant by translation along  $x$  (which hence effectively maps to a two-dimensional problem for the Poisson equation and a one-dimensional one for the quantum problem). We obtain  $V(|x| \gg 10, y, 0) \equiv V_A(y)$ . Second, we solve the problem deep inside the central region, assuming that the potential is not affected by the leads (and hence is also invariant by translation along  $x$ ). We obtain  $V(|x| \ll 10, y, 0) \equiv V_B(y)$ . An example of the obtained self-consistent potentials  $V_B(y)$  (left) and  $V_A(y)$  (right) is shown in Fig. 6 for  $V_t = -0.43$  V,  $V_m = -0.495$  V, and  $V_l = -0.45$  V. In the last step, we describe the potential in the transition regions ( $x \in [-9.2, -6.9]$  and  $x \in [6.9, 9.2]$ ) by performing an interpolation between  $V_A(y)$  and  $V_B(y)$ .

The density of the gas is  $\sim 3.2 \times 10^{11} \text{ cm}^{-2}$ , which corresponds to a Fermi wavelength  $\lambda_F \approx 45$  nm. Since the transition region is long compared to  $\lambda_F$ , the transition is adiabatic, and we observe a very small reflection probability. We also have to check that the mode coming from  $L \uparrow$  is fully transmitted into the mode of  $R \uparrow$  and  $R \downarrow$  and is not leaked into  $L \downarrow$ . Otherwise, it would create Fabry-Pérot interferences between both potential transitions which will compete with the Mach-Zehnder interferometry. This is achieved by a smooth transition of the potential.

### C. dc and ac characterization

Once the electrostatic potential is known, we calculate the transmission probabilities for the various conducting channels. We have used  $V_t = -0.43$  V,  $V_l = -0.45$  V, and  $V_m = -0.495$  V, so that five propagating channels are open in each lead, and ten channels are open in the central region (a typical experimental situation). The left panel of Fig. 7 shows an example of the band structure of the central region, where we have used matching colors to identify the symmetric-antisymmetric pairs. The right panel of Fig. 7 shows  $E(k=0)$  for the various modes, which allows us to identify the propagating channels [ $E(k=0) < 0$ ] and evaluate the splitting between the symmetric and antisymmetric components. Figure 8 shows the dc conductance (at zero temperature) as a function of the tunneling voltage  $V_t$  (lower panel) obtained with KWANT [33]. The top panel shows the contributions from the different propagating channels. The strongest oscillating signal is obtained close to the onset of the opening of a new channel where the two momenta for the symmetric and antisymmetric channels are the most different.

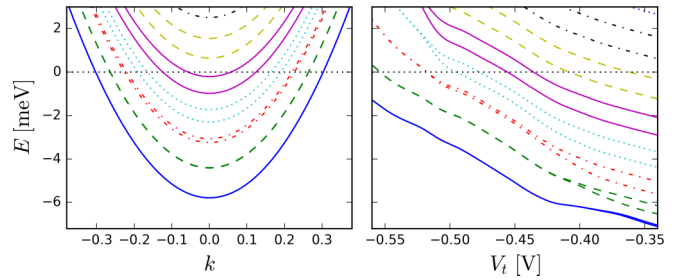


FIG. 7. Structure of the subbands in the central region. Left: Energy dispersion  $E(k)$  versus  $k$  for  $V_t = -0.43$  V. The bands that cross the Fermi energy  $E = E_F = 0$  correspond to propagating channels. Right: Transverse energies  $E(k=0)$  of the different modes as a function of the tunneling voltage  $V_t$ . The bands below the Fermi energy are propagating. Parameters:  $V_m = -0.495$  V and  $V_l = -0.45$  V for both panels. Symmetric-antisymmetric mode pairs are plotted with similar colors and line styles.

### D. Rectification spectroscopy

The total number of orbitals is now rather large ( $\sim 2 \times 10^6$ ), so a direct time-dependent calculation is prohibitive. But discussion of Sec. IV C shows that we can use Eq. (7) and get the same results with much less computational time. In order to obtain the rectification current one requires the calculation of the total transmission probability

$$D_{ab}(E) = \sum_{\alpha \in a, \beta \in b} |d_{\alpha\beta}(E)|^2, \quad (19)$$

where the sum is taken over all the propagating channels of the corresponding electrode. An example of such a calculation using KWANT [33] is shown in Fig. 9 together with the detailed contributions of the different channels. The curve  $D_{ab}(E)$ , antisymmetrized around the Fermi level, provides the information for the calculation of the rectified current response to

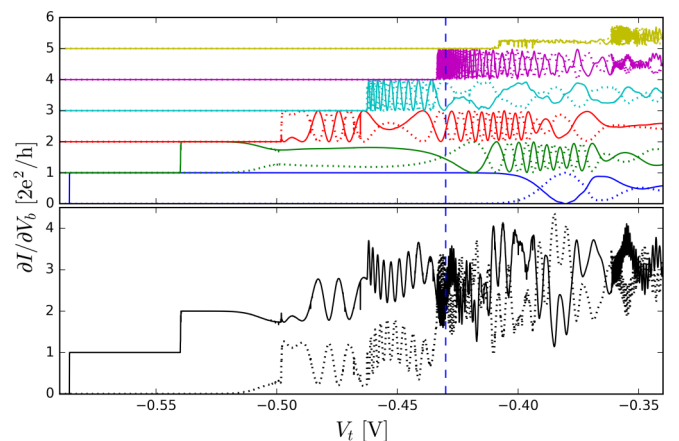


FIG. 8. Bottom: dc differential conductance  $\partial I / \partial V_b$  as a function of the central gate voltage  $V_t$  for  $V_l = -0.45$  V and  $V_m = -0.495$  V. The voltage bias  $V_b$  is applied to the upper left contact  $L_t$ , while the other three are grounded. The current is measured in the upper right contact  $R_t$  (solid lines,  $\partial I_t / \partial V_b$ ) and in the lower right contact  $R_b$  (dashed line,  $\partial I_b / \partial V_b$ ). Top: contribution of  $2e^2/h$  for the individual propagating channels, shifted by multiples of  $2e^2/h$  for clarity. Calculations were performed at zero temperature.

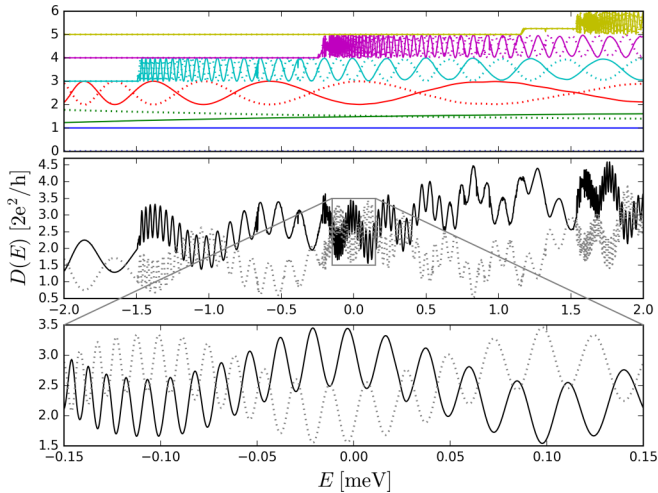


FIG. 9. Middle: total transmission probability  $D(E)$  [solid line,  $D_{\uparrow\uparrow}(E)$ ; dashed line,  $D_{\downarrow\downarrow}(E)$ ] vs energy  $E$ , where  $E$  is measured relative to the Fermi energy  $E_F$ . Top: contribution from the individual propagating channels, shifted by multiples of  $2e^2/h$  for clarity. Bottom: zoom of the middle panel. Parameters:  $V_l = -0.43$  V,  $V_r = -0.45$  V, and  $V_m = -0.495$  V for all panels.

an ac drive, as can be seen from the following reformulation of Eq. (7):

$$\bar{I}_b = \frac{e}{h} \sum_{n>0} |P_n|^2 \int dE [D_{ba}(E-n) - D_{ba}(E_n)] \times [f_a(E_n) - f_a(E-n)], \quad (20)$$

where  $E_n = E + n\hbar\omega/2$ . Conversely, Eq. (20) shows that the rectification response can be used to reconstruct the antisymmetrized transmission probability of the device. To reconstruct the full transmission probability, including the symmetric part, calculations and measurements for different Fermi levels (using, e.g., a back gate) are necessary.

The resulting rectified current for the realistic model is shown in Fig. 10. Figure 10 is qualitatively similar to the idealized model despite the fact that it includes a realistic modeling of the electrostatic potential, multiple open channels (five), and a finite temperature (20 mK). This is a strong indication of the robustness of this type of spectroscopy.

An important aspect of the multichannel model is that different channels (with different scales  $\tau$ ) contribute to the rectified current with contributions of the order of  $1/\tau$ , so the fastest channels have larger contributions. However, this does not prevent one from observing the slowest channels since the scales at which the different contributions vary is also very different [as can be inferred by an inspection of Eq. (9a)]. In order to bring the different contributions to the same scale, it can be advantageous to plot the derivative of the current  $\partial\bar{I}/\partial V_0$  instead of the current itself. This is typically performed experimentally using a lock-in technique. The signal can be further amplified by plotting the antisymmetric signal  $\partial\bar{I}_{\uparrow}/\partial V_0 - \partial\bar{I}_{\downarrow}/\partial V_0$  with respect to the two outputs in order to subtract any spurious signal coming from other rectification processes. Indeed, the multichannel realistic model contains another source of rectification current coming from the opening of new channels which give rise

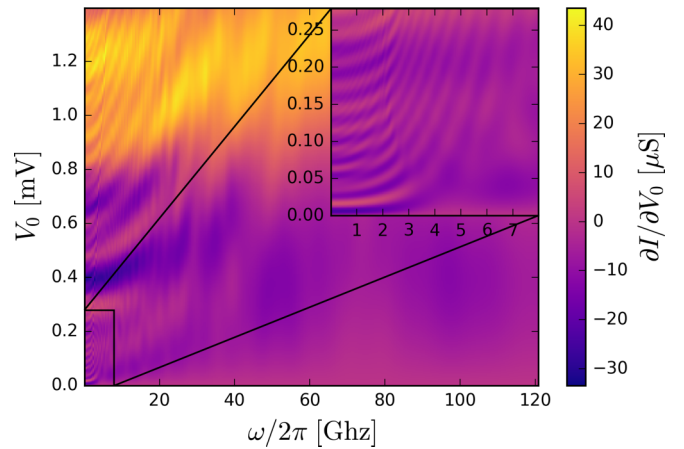


FIG. 10. Realistic microscopic model. Color map of  $\partial\bar{I}_{\uparrow}/\partial V_0 - \partial\bar{I}_{\downarrow}/\partial V_0$  versus voltage amplitude  $V_0$  and frequency  $\omega/2\pi$ . The inset shows a zoom of the main panel. Two channels with  $\tau = 220$  ps (oscillations visible in the inset) and  $\tau = 19$  ps (oscillations visible in the main panel) dominate the signal. Calculations were performed at 20 mK.

to plateaus in the rectification current. These plateaus are very conveniently subtracted by looking at the antisymmetric signal  $\partial\bar{I}_{\uparrow}/\partial V_0 - \partial\bar{I}_{\downarrow}/\partial V_0$ .

The data in Fig. 10 correspond to five pairs of propagating channels with  $\tau = 220$ , 19, and 3 ps and two very fast channels with  $\tau \ll 1$  ps. With current experimental capabilities, the two interesting pairs that may be used for flying qubits are the two slowest,  $\tau = 220$  ps and 19 ps. It is interesting that despite the presence of the three faster pairs, the spectroscopy lines of these two pairs are clearly visible in Fig. 10: at these scales, the three fast pairs contribute only to a global background. The two characteristic times  $\tau = 220$  and 19 ps can be directly extracted by fitting the low-frequency ( $<10$  GHz) and high-frequency ( $<100$  GHz) parts of the diagram.

## VI. DISCUSSION AND CONCLUSION

The experimental observation of the features shown in Fig. 10 would provide the first direct measure of the characteristic times of the device and validate the possibility for the dynamical probing of an interference pattern at high frequency. This is a key step on the route toward further quantum manipulation with voltage pulses and the first full-fledged electronic flying qubit [5].

Another important aspect which is at stake is our ability to make accurate models and predictive simulations for high-frequency quantum transport. At the experimental level, the electrostatic gates are controlled with voltages of the order of 1 V, while the equilibrium electrostatic potential seen by the electrons is of the order of several mV, i.e., 2–3 orders of magnitude smaller (see, e.g., Fig. 6). Hence, the construction of accurate models must go through a precise understanding of the combined electrostatic-quantum problem in the presence of high-frequency dynamics. Conversely, the physics of these systems depends on the precise interplay between these two physics. Being in the position to make quantitative predictions for these systems would allow one

to design much more optimum geometries and experimental protocols, which would have a decisive impact on the development of the field. This paper presented a step in this direction.

Our understanding of high-frequency quantum transport, pulse propagation, and dynamical interferometry (the ingredients of electronic flying qubit architectures) is mostly based so far on noninteracting models. As the experiments progress toward the exploration of this new physics, the modeling will require new aspects to be treated more accurately. Future work will include a proper treatment of the electron-electron interactions at the random-phase approximation level [38] and

beyond as well as the modelization of the different channels for decoherence. Indeed, understanding what sets the fundamental limit of coherence in these systems will probably be one of the most interesting challenges of the field in the years to come.

### ACKNOWLEDGMENTS

This work was supported by the ANR Fully Quantum Project No. ANR-16-CE30-0015-02, ANR QTERA Project No. ANR-15-CE24-0007-02 and U.S. Office of Naval Research. We thank C. Bäuerle for useful discussions.

- 
- [1] D. Loss and D. P. DiVincenzo, Quantum computation with quantum dots, *Phys. Rev. A* **57**, 120 (1998).
- [2] Y. Zavoisky, Paramagnetic relaxation of liquid solutions for perpendicular fields, *J. Phys USSR* **9**, 211 (1945).
- [3] E. Knill, R. Laflamme, and G. J. Milburn, A scheme for efficient quantum computation with linear optics, *Nature (London)* **409**, 46 (2001).
- [4] D. Maxein and J. Laurat, Trapped ion to flying qubit, *Nat. Photonics* **7**, 169 (2013).
- [5] C. Bäuerle, D. C. Glatli, T. Meunier, F. Portier, P. Roche, P. Roulleau, S. Takada, and X. Waintal, Coherent control of single electrons: A review of current progress, *Rep. Prog. Phys.* **81**, 056503 (2018).
- [6] G. Haack, M. Moskalets, J. Splettstoesser, and M. Büttiker, Coherence of single-electron sources from Mach-Zehnder interferometry, *Phys. Rev. B* **84**, 081303 (2011).
- [7] G. Fève, P. Degiovanni, and T. Jolicoeur, Quantum detection of electronic flying qubits in the integer quantum Hall regime, *Phys. Rev. B* **77**, 035308 (2008).
- [8] Y. Ji, Y. Chung, D. Sprinzak, M. Heiblum, D. Mahalu, and H. Shtrikman, An electronic Mach-Zehnder interferometer, *Nature (London)* **422**, 415 (2003).
- [9] P. Roulleau, F. Portier, P. Roche, A. Cavanna, G. Faini, U. Gennser, and D. Mailly, Direct Measurement of the Coherence Length of Edge States in the Integer Quantum Hall Regime, *Phys. Rev. Lett.* **100**, 126802 (2008).
- [10] T. Bautze, C. Süssmeier, S. Takada, C. Groth, T. Meunier, M. Yamamoto, S. Tarucha, X. Waintal, and C. Bäuerle, Theoretical, numerical, and experimental study of a flying qubit electronic interferometer, *Phys. Rev. B* **89**, 125432 (2014).
- [11] M. Yamamoto, S. Takada, C. Bäuerle, K. Watanabe, A. D. Wieck, and S. Tarucha, Electrical control of a solid-state flying qubit, *Nat. Nanotechnol.* **7**, 247 (2012).
- [12] D. S. Wei, T. van der Sar, J. D. Sanchez-Yamagishi, K. Watanabe, T. Taniguchi, P. Jarillo-Herrero, B. I. Halperin, and A. Yacoby, Mach-Zehnder interferometry using spin- and valley-polarized quantum Hall edge states in graphene, *Sci. Adv.* **3**, e1700600 (2017).
- [13] J. Dubois, T. Jullien, F. Portier, P. Roche, A. Cavanna, Y. Jin, W. Wegscheider, P. Roulleau, and D. C. Glatli, Minimal-excitation states for electron quantum optics using levitons, *Nature (London)* **502**, 659 (2013).
- [14] E. Bocquillon, V. Freulon, J.-M. Berroir, P. Degiovanni, B. Plaças, A. Cavanna, Y. Jin, and G. Fève, Coherence and indistinguishability of single electrons emitted by independent sources, *Science* **339**, 1054 (2013).
- [15] R. P. G. McNeil, M. Kataoka, C. J. B. Ford, C. H. W. Barnes, D. Anderson, G. A. C. Jones, I. Farrer, and D. A. Ritchie, On-demand single-electron transfer between distant quantum dots, *Nature (London)* **477**, 439 (2011).
- [16] G. Fève, A. Mahé, J.-M. Berroir, T. Kontos, B. Plaças, D. C. Glatli, A. Cavanna, B. Etienne, and Y. Jin, An on-demand coherent single-electron source, *Science* **316**, 1169 (2007).
- [17] B. Gaury and X. Waintal, Dynamical control of interference using voltage pulses in the quantum regime, *Nat. Commun.* **5**, 3844 (2014).
- [18] P. P. Hofer and C. Flindt, Mach-Zehnder interferometry with periodic voltage pulses, *Phys. Rev. B* **90**, 235416 (2014).
- [19] B. Gaury, J. Weston, and X. Waintal, The a.c. Josephson effect without superconductivity, *Nat. Commun.* **6**, 6524 (2015).
- [20] M. L. Polianski and P. W. Brouwer, Pumped current and voltage for an adiabatic quantum pump, *Phys. Rev. B* **64**, 075304 (2001).
- [21] P. W. Brouwer, Rectification of displacement currents in an adiabatic electron pump, *Phys. Rev. B* **63**, 121303 (2001).
- [22] M. G. Vavilov, L. DiCarlo, and C. M. Marcus, Photovoltaic and rectification currents in quantum dots, *Phys. Rev. B* **71**, 241309 (2005).
- [23] L. Arrachea and M. Moskalets, Relation between scattering-matrix and Keldysh formalisms for quantum transport driven by time-periodic fields, *Phys. Rev. B* **74**, 245322 (2006).
- [24] S. P. Giblin, M. Kataoka, J. D. Fletcher, P. See, T. J. B. M. Janssen, J. P. Griffiths, G. A. C. Jones, I. Farrer, and D. A. Ritchie, Rectification in mesoscopic alternating current-gated semiconductor devices, *J. Appl. Phys.* **114**, 164505 (2013).
- [25] M. Martínez-Mares, C. H. Lewenkopf, and E. R. Mucciolo, Statistical fluctuations of pumping and rectification currents in quantum dots, *Phys. Rev. B* **69**, 085301 (2004).
- [26] S. Takada, C. Bäuerle, M. Yamamoto, K. Watanabe, S. Hermelin, T. Meunier, A. Alex, A. Weichselbaum, J. von Delft, A. Ludwig, A. D. Wieck, and S. Tarucha, Transmission Phase in the Kondo Regime Revealed in a Two-Path Interferometer, *Phys. Rev. Lett.* **113**, 126601 (2014).
- [27] S. Takada, M. Yamamoto, C. Bäuerle, K. Watanabe, A. Ludwig, A. D. Wieck, and S. Tarucha, Measurement of the transmission phase of an electron in a quantum two-path interferometer, *Appl. Phys. Lett.* **107**, 063101 (2015).



- [28] J. Weston and X. Waintal, Towards realistic time-resolved simulations of quantum devices, *J. Comput. Electron.* **15**, 1148 (2016).
- [29] M. V. Moskalets, *Scattering Matrix Approach to Non-stationary Quantum Transport* (Imperial College Press, London, 2011).
- [30] O. Shevtsov and X. Waintal, Numerical toolkit for electronic quantum transport at finite frequency, *Phys. Rev. B* **87**, 085304 (2013).
- [31] B. Gaury, J. Weston, M. Santin, M. Houzet, C. Groth, and X. Waintal, Numerical simulations of time-resolved quantum electronics, *Phys. Rep.* **534**, 1 (2014).
- [32] G. Roussely, E. Arrighi, G. Georgiou, S. Takada, M. Schalk, M. Urdampilleta, A. Ludwig, A. D. Wieck, P. Armagnat, T. Kloss, X. Waintal, T. Meunier, and C. Bäuerle, Unveiling the bosonic nature of an ultrashort few-electron pulse, *Nat. Commun.* **9**, 2811 (2018).
- [33] C. W. Groth, M. Wimmer, A. R. Akhmerov, and X. Waintal, Kwant: A software package for quantum transport, *New J. Phys.* **16**, 063065 (2014).
- [34] M. Büttiker, H. Thomas, and A. Prêtre, Mesoscopic capacitors, *Phys. Lett. A* **180**, 364 (1993).
- [35] J. Weston and X. Waintal, Linear-scaling source-sink algorithm for simulating time-resolved quantum transport and superconductivity, *Phys. Rev. B* **93**, 134506 (2016).
- [36] C. Bäuerle (private communication).
- [37] Edited by A. Logg, K.-A. Mardal, and G. N. Wells, *Automated Solution of Differential Equations by the Finite Element Method* (Springer, Berlin, 2012).
- [38] T. Kloss, J. Weston, and X. Waintal, Transient and Sharvin resistances of Luttinger liquids, *Phys. Rev. B* **97**, 165134 (2018).